The "Second Stalk" of *Escherichia coli* ATP Synthase: Structure of the Isolated Dimerization Domain[†,‡]

Paul A. Del Rizzo, Yumin Bi, Stanley D. Dunn, and Brian H. Shilton*

Department of Biochemistry, University of Western Ontario, London, ON N6A 5C1, Canada

Received February 26, 2002

ABSTRACT: The *b* subunit of *E. coli* F_0F_1-ATPase links the peripheral F_1 subunits to the membrane-integral F_0 portion and functions as a "stator", preventing rotation of F_1. The *b* subunit is present as a dimer in ATP synthase, and residues 62−122 are required to mediate dimerization. To understand how the *b* subunit dimer is formed, we have studied the structure of the isolated dimerization domain, b_{62-122}. Analytical ultracentrifugation and solution small-angle X-ray scattering (SAXS) indicate that the b_{62-122} dimer is extremely elongated, with a frictional ratio of 1.60, a maximal dimension of 95 Å, and a radius of gyration of 27 Å, values that are consistent with an α-helical coiled-coil structure. The crystal structure of b_{62-122} has been solved and refined to 1.55 Å. The protein crystallized as an isolated, monomeric α helix with a length of 90 Å. Combining the crystal structure of monomeric b_{62-122} with SAXS data from the dimer in solution, we have constructed a model for the b_{62-122} dimer in which the two helices form a coiled coil with a right-handed superhelical twist. Analysis of *b* sequences from *E. coli* and other prokaryotes indicates conservation of an undecad repeat, which is characteristic of a right-handed coiled coil and consistent with our structural model. Mutation of residue Arg-83, which interrupts the undecad pattern, to alanine markedly stabilized the dimer, as expected for the proposed two-stranded, right-handed coiled-coil structure.

ATP synthase is a molecular motor that couples the movement of protons to the synthesis of ATP. In the rotational model of the enzyme, protons travel down an electrochemical gradient and drive rotation of a ring of *c* subunits in the membrane-integral F_0 portion. This rotation is transmitted to the membrane-peripheral F_1 portion of the enzyme through the "central stalk". As it rotates, the central stalk interacts sequentially with three *β* subunits in the F_1 portion to alter their conformation. It is these conformational changes that drive the synthesis of ATP from ADP and inorganic phosphate. In this model of catalysis, the ring of α and *β* subunits must be prevented from sliding off the central stalk, and it must be held stationary relative to the rotating ring of *c* subunits in the membrane. The function of the *b* subunit (the "second stalk" of ATP synthase) is to link the F_1 portion of the enzyme to the F_0 portion, thereby keeping the F_1−F_0 complex together at the membrane and coupling ATP synthesis to proton translocation. There are a number of reviews on ATP synthase structure and mechanism (*1*−*4*).

The second stalk may have a more complex functional role than providing a simple tether between the F_0 and F_1 portions of the enzyme. First, the rotating ring of the F_0 portion contains, on average, 10 *c* subunits (*5*); as each *c* subunit rotates past the *a* subunit, one proton is translocated across the membrane. Since three ATP molecules are produced for each rotation of the central stalk, there must be a nonintegral number of protons used to produce each ATP molecule. The complex as a whole must therefore allow for a certain degree of "play" between the F_0 and F_1 portions. A second point is that the conformation of the nucleotide binding sites of F_1 may be affected by binding of the *b* subunit to the exterior surface (*6*). Additionally, the structure of the *b* subunit is of interest because each protomer must make unique contacts with the surfaces of the α, *β*, and *δ* subunits, none of which possess a 2-fold symmetry axis.

The second stalk of the *E. coli* ATP synthase is a homodimer of *b* subunits that is composed of four domains. The N-terminal domain spans the membrane and interacts with the *a* subunit. It is followed by the "tether domain", the "dimerization domain", and the C-terminal *δ*-binding domain (see ref 7 for a recent review). In the present work, we have focused our attention on the structure of the dimerization domain b_{62-122}. We use small-angle X-ray scattering to show that this portion of the molecule forms an extended dimer in solution, approximately 95 Å long with a radius of gyration of 27 Å. A high-resolution crystal

---

[†] S.D.D. is supported by Canadian Institutes for Health Research Grant MT-10237, and B.H.S. is supported by Canadian Institutes for Health Research Grant MT-15624 and Natural Sciences and Engineering Research Council Grant 21749-1999. P.D.R. is supported by a Natural Sciences and Engineering Research Council studentship. The macromolecular X-ray facility at The University of Western Ontario was financed with grants from the Canada Foundation for Innovation, Ontario Challenge Fund, and Western's Academic Development Fund. Sedimentation and CD studies were carried out in the U.W.O. Biomolecular Interactions and Conformations Facility, supported by a Multiuser Maintenance and Equipment Grant from the Canadian Institutes of Health Research. Use of the Advanced Photon Source was supported by the U.S. Department of Energy, Basic Energy Sciences, Office of Science, under Contract No. W-31-109-ENG-38. BioCAT is a National Institutes of Health supported Research Center, Grant RR-08630.

[‡] Coordinates for the b_{62-122} monomer structure have been deposited in the Protein Data Bank with the identification 1L2P.

* To whom correspondence should be addressed. Telephone: 519-661-4124. Fax: 519-661-3175. E-mail: bshilton@uwo.ca.

10.1021/bi025736i CCC: $22.00

structure of monomeric b_{62-122}, X-ray scattering data, sequence analysis, and results from mutagenesis are all consistent with a model in which the two b_{62-122} helices associate to form a coiled coil with a right-handed superhelical twist.

EXPERIMENTAL PROCEDURES

Plasmid Construction. Recombinant DNA procedures were carried out using methods described by Sambrook et al. (*8*). Plasmid pSD149, which encodes residues 62−122 of the *b* subunit of ATP synthase, was produced by inserting the product of a primed synthesis reaction utilizing oligonucleotides with sequences 5′ CCGGAATTCTGGAGGATTTTACATATG 3′ and 5′ CACGCTTAAGCTGATCAGTCATATGTAAAATC 3′ into plasmid pSD129 (*9*) using the *Eco*RI and *Afl*II sites. Mutations introducing cysteine residues into the sequence at positions 68, 92, and 103 were transferred from plasmids pDM11 (*10*), pSC2 (*11*), and pDM52 (*9*) to pSD149, utilizing unique pairs of restriction enzyme sites to produce plasmids pSD155, pSD173, and pSD156, respectively. Mutations intoducing alanine residues into positions 82, 83, and 98 were constructed by a polymerase chain reaction and were cloned into pSD149 using appropriate restriction enzyme sites to produce plasmids pSD182, pSD180, and pSD185, respectively. The mutation encoding alanine at position 83 was introduced into plasmid pSD129 to produce pSD187, which expresses b_{53-122} with the R83A mutation.

Protein Expression and Purification. The purification of b_{53-122} has been described previously (*9*). Similar procedures were used for the R83A mutant protein. b_{62-122} and point mutants were expressed from plasmids in strain MM294 using described procedures (*9, 10*). Cells were broken by passage through a French pressure cell at 20 000 psi after the addition of phenylmethylsulfonyl fluoride to a final concentration of 1 mM. Removal of cellular debris, membranes, and ribosomes was completed by ultracentrifugation at 38 000 rpm for 1.5 h using a Beckman Ti-45 rotor. Proteins precipitated between 65 and 100% saturation of ammonium sulfate were redissolved in 20 mM Tris-HCl, pH 8.0, and 1 mM EDTA (TE buffer) and dialyzed to remove ammonium sulfate. The dialyzate was applied to a column of DEAE-Sepharose (2.5 cm × 20 cm) equilibrated in the same buffer and eluted with 300 mL of the same buffer. b_{62-122} protein eluted shortly after the solvent front, and most contaminant proteins remained bound to the resin. Fractions obtained were characterized by SDS−PAGE, and the best fractions were pooled and acidified with 5% acetic acid to a final pH of 5.0. This sample was then applied to a CM-Sepharose (1.5 cm × 20 cm) column equilibrated with 30 mM sodium acetate, pH 5.0, and eluted with a linear gradient of 100−600 mM NaCl. Fractions with high purity were pooled, dialyzed against 30 mM sodium acetate, pH 5.0, and applied to an SP-Sepharose Hi-Trap column (1 mL, Pharmacia) for concentration. Protein was eluted with 1 M NaCl, and the most concentrated fractions were pooled and dialyzed against water.

Expression and purification of the cysteine-containing mutants (A68C, A92C, and A103C) were done by the same procedure as outlined above, with the addition of 1 mM dithiothreitol to all buffers after the ammonium sulfate precipitation.

Expression and purification of the b_{62-122}R83A construct was carried out as described for the wild-type construct, with minor changes. An SP-Sepharose-HR (Pharmacia; 1.6 cm × 22 cm) FPLC column was used in place of the CM-Sepharose column. Protein was eluted with a linear gradient of 0−1 M NaCl in 30 mM sodium acetate buffer, pH 5.0, to yield pure b_{62-122}R83A as determined by SDS−PAGE.

Circular Dichroism Spectroscopy. CD spectra were collected using a Jasco J-810 spectropolarimeter with jacketed cells of 0.1 or 1 mm path length. Proteins were dialyzed into sodium phosphate buffers as specified and diluted with the same buffer to obtain the desired concentrations. Far-UV wavelength scans were collected from 190 to 250 nm in 0.5 nm steps. Temperature scans were collected at 222 nm in 1 °C steps with a temperature ramp speed of 1 °C per minute. Complete spectra were collected every 5 °C. CD measurements were converted to mean residue ellipticity in the standard manner.

Analytical Ultracentrifugation. Analytical ultracentrifugation was carried out in a Beckman XL-A instrument with a four-hole An-60Ti rotor. The b_{53-122} constructs contained aromatic residues and were observed at 280 nm. The b_{62-122} constructs lacked aromatic residues and were observed at wavelengths between 230 and 245 nm. The buffer used in each set of experiments is specified in the figure captions.

Sedimentation equilibrium runs utilized six-sector cells with Epon charcoal centerpieces at rotor speeds ranging from 15 000 to 30 000 rpm. Absorbance measurements were taken in 0.002 cm radial steps and averaged over 10 observations. Equilibrium was ascertained by comparing scans taken at 2 h intervals. Software supplied by Beckman was used for data processing and curve fitting. Partial specific volumes were calculated using the method of Cohn and Edsall (*12*).

Sedimentation velocity analyses were carried out in Epon charcoal double-sector cells at a rotor speed of 60 000 rpm. Scans were taken at 10 min intervals using a step size of 0.005 cm and averaged over five observations. Sedimentation coefficients were calculated by the SVEDBERG program (*13*) using the modified Fujita−MacCosham model fitted for a single species.

Crystal Structure Solution. Data were processed, scaled, and merged with Denzo and HKL (*14*). Experimental phase calculation, refinement, and map calculations were performed using MLPHARE and other programs in the CCP4 suite (*15*). The crystallographic model was built using the program O (*16*), and refinement along with map calculation using model phases was carried out with CNS (*17*). Both O (*16*) and SwissPDBViewer (*18*) were used to construct models for the b_{62-122} dimer and to produce molecular graphics.

Crystals were grown using sitting drop vapor diffusion by mixing equal volumes of b_{62-122} at 25 mg mL^{-1} and a reservoir solution consisting of 45% 2-propanol and 30% 2-methyl-2,4-pentanediol (MPD).[1] Crystals were flash-frozen in a nitrogen gas stream at 100 K, and all data were collected at 100 K. Heavy-atom soaks were carried out in 50% 2-propanol, 30% MPD, and 50 mM NaCl, using 1 mM ethyl mercury phosphate (EMP; Noah Technologies, San Antonio,

---

[1] Abbreviations: MPD, 2-methyl-2,4-pentanediol; SAXS, small-angle X-ray scattering; EMP, ethylmercury phosphate; rms, root-mean-square.

TX). The soaks were conducted in the presence of 50 mM NaCl and back-soaked in EMP-free solution to minimize nonspecific adsorption of EMP to the protein.

The protein crystallized in space group $P2_12_12$ with unit cell dimensions $a = 36.7$ Å, $b = 40.7$ Å, and $c = 42.3$ Å. Three cysteine-containing b_{62-122} proteins were used for MIRAS phasing: b_{62-122}A68C, b_{62-122}A92C, and b_{62-122}A103C. In all cases, isomorphous and anomalous difference Patterson maps contained peaks with heights from 4σ to 10σ (where σ is the peak height divided by the rms deviation of the map) that were used to manually calculate the positions of mercury atoms. Phases from the b_{62-122}A68C derivative were the best determined (Table 2), and we attempted to use these phases to calculate difference Fourier maps for the other derivatives. However, the difference Fourier maps calculated in this manner did not have peaks that rose significantly above background. Therefore, the three derivatives were put on a common origin as follows. For each derivative, the anomalous signal was used to distinguish the correct hand, narrowing possible choices for the origin from 16 to 8. Initial phases were calculated with the b_{62-122}A68C derivative, and then isomorphous and anomalous data from the b_{62-122}A103C derivative were incorporated into the phase refinement, which was repeated using each of the eight possible origins; the position that yielded the highest isomorphous and anomalous occupancies was chosen as having the correct origin. This process was repeated with the b_{62-122}A92C derivative data. Once all three mercury positions were placed on a common origin, the three data sets, including both isomorphous and anomalous data, were used to refine the phases, yielding a 2.3 Å resolution electron density map.

Small-Angle X-ray Scattering. Scattering measurements from b_{62-122} and b_{53-122} were made at the European Molecular Biology Laboratory Outstation at the Deutsches Elektronen-Synchrotron (Hamburg, Germany), beamline X33 (*19*), at 15 °C using radiation with a wavelength of 1.5 Å and a path length of 1 mm. Measurements were made with a quadrant segment-shaped multiwire detector (*20*). Sample–detector distances of 1.2 m (high angle) and 3 m (low angle) were used to cover the range of momentum transfer ($S = 2\sin\theta/\lambda$, where 2θ is the scattering angle) from 0.003 to 0.085 Å^{-1}. Fifteen successive 1 min exposures were recorded for each sample; there was no evidence of protein degradation over this time interval. Recording of each protein sample was preceded and followed by recording from the buffer alone; these buffer measurements were compared and provided a check on beam properties and the cleanliness of the cell between readings of protein solutions. Averaging of frames, corrections for detector response and beam intensity, and buffer subtraction were done using the programs SAPOKO (Svergun, D.I, and Koch, M. H. J., unpublished) and OTOKO (*21*). Scattering from the b_{62-122}R83A mutant was measured at BioCAT (beamline 18ID) of the Advanced Photon Source. In this case, the sample temperature was approximately 20 °C and the protein solution was moved continuously through a 1 mm quartz capillary during the course of the measurement. Data were collected at 2.78 m and 25.5 cm using a CCD detector, with X-rays at a wavelength of 1.03 Å, to cover the momentum transfer range 0.001 Å^{-1} < S < 0.3 Å^{-1}. The two-dimensional data were reduced using the program Fit2D (*22–24*), and further data processing (correction for ion chamber readings) was carried out using Microsoft Excel spreadsheets.

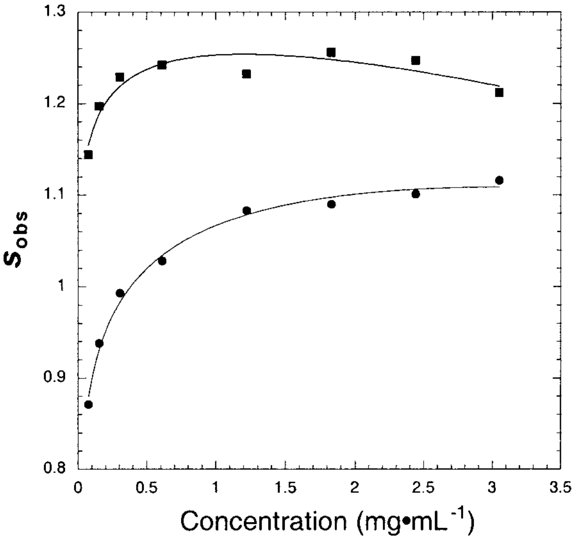

FIGURE 1: Sedimentation analysis of b_{62-122}. Sedimentation velocity analysis of wild-type b_{62-122} (circles) or b_{62-122}R83A (squares) at a range of protein concentrations was carried out using double sector cells at 60 000 rpm and 20 °C. The buffer contained 25 mM sodium phosphate, pH 7.0, and 50 mM NaCl. Cells were scanned at wavelengths between 229 and 245 nm depending on protein concentration. Data were analyzed using the SVEDBERG program (*13*) to obtain the observed sedimentation coefficient.

Models of the b_{62-122} dimer, excluding crystallographic water molecules, were evaluated on the basis of their fit to experimental SAXS data using the program CRYSOL (*25*), with a solvent density of 0.33 electrons/Å^3, using default limits for the contrast of the hydration shell and average displaced solvent volume per atomic group. The target function for CRYSOL is the χ^2 value, which is a measure of the agreement between the theoretical scattering from a model and the experimental data,

$$\chi^2 = \frac{1}{N-1}\sum_{j=1}^{N}\left|\frac{I(S_j) - I_{\exp}(S_j)}{\sigma(S_j)}\right|^2 \qquad (1)$$

where for each momentum transfer value S_j, $I(S_j)$ is the theoretical scattering, $I_{\exp}(S_j)$ is the experimentally observed scattering, and $\sigma(S_j)$ is the error for the experimental measurement.

Other Methods. SDS–polyacrylamide gels of the b_{62-122} constructs were done using 15% polyacrylamide gels and the Tris-Tricine buffer system as described previously (*9*). Protein concentrations were determined by Advanced Protein Assay (Cytoskeleton, Inc.) and standardized against a reference sample determined by quantitative amino acid analysis at the Alberta Peptide Institute.

RESULTS AND DISCUSSION

Initial Characterization of b_{62-122}. Previous deletion studies revealed that forms of the *b* subunit beginning at residue Asp-53 were dimeric while those beginning at Lys-67 were monomeric (*10*). To further define the N-terminal boundary of the region essential for dimerization, a construct containing residues Thr-62 through Lys-122 (b_{62-122}) was prepared. This sequence contains no aromatic residues or leader sequence,

Table 1: Data Collection Statistics for Native Crystals

	native 1[a]	native 2	A68C	A92C	A103C[b]
cell axes					
a (Å)	35.65	35.29	35.47	35.90	35.55
b (Å)	40.70	40.71	40.88	41.27	41.40
c (Å)	42.30	42.33	42.19	42.19	42.45
resolution (Å)	1.55	2.45	2.5	2.6	2.0
unique reflections	9455	2479	2347	2063	4550
redundancy[c]	5.4	6.4	4.1	6.5	6.1
% completeness[c,d]	93.5 (83.1)	96.3 (94.6)	97.4 (93.1)	91.0 (84.3)	93.5 (87.0)
R_{merge}[d]	2.7 (11.7)	5.6 (16.1)	6.5 (18.9)	8.1 (23.7)	6.3 (15.7)

[a] Collected at CHESS beamline F1, $\lambda = 0.9920$ Å. [b] Collected at CHESS beamline A1, $\lambda = 0.9243$ Å. [c] For reflections with $I > \sigma I$. [d] Values in parentheses correspond to the highest resolution shell.

Table 2: Data Collection and Phasing Statistics for Derivative Crystals

	A68C-EMP	A92C-EMP	A103C-EMP
cell axes			
a (Å)	35.38	35.68	35.24
b (Å)	40.63	41.03	41.15
c (Å)	42.24	42.19	42.36
resolution (Å)	2.5	2.2	2.3
unique reflections	2384	3376	3214
redundancy[a]	11.3	13.1	13.2
% completeness[a,b]	98.7 (92.7)	97.2 (77.6)	99.4 (99.0)
R_{merge}[b]	9.2 (22.7)	7.0 (16.2)	5.4 (20.9)
R_{iso}[c]	31.7	29.7	29.6
phasing power[d] (centric/acentric)	2.2/2.6	1.1/1.4	1.5/1.9
Cullis *R*[d] (centric/acentric)	0.46/0.56	0.71/0.81	0.61/0.69
Cullis *R* anomalous[d]	0.60	0.64	0.84
figure of merit[d] (centric/acentric/overall)	0.81/0.75/0.76		

[a] For reflections with $I > \sigma I$. [b] Values in parentheses correspond to the highest resolution shell. [c] As output by the program SCALEIT (*15*) for data from 12.5 to 3.5 Å resolution against "native 2" data, collected on a rotating anode source (Table 1). [d] As output by the program MLPHARE (*15*) to 2.3 Å resolution.

and mass spectrometry gave a mass of 7044 Da, confirming removal of the initiating methionine residue.

A number of lines of evidence showed that the b_{62-122} polypeptide formed dimers in solution but more weakly than the previously characterized b_{53-122} construct (*26*). The observed sedimentation coefficient increased with protein concentration in a manner characteristic of conversion from predominantly monomer at low protein concentrations to predominantly dimer at higher concentrations (Figure 1). Analysis of molecular weight by sedimentation equilibrium ultracentrifugation also yielded values dependent on protein concentration; at a starting concentration of 0.6 mg mL^{-1}, the system gave an average molecular weight of 10 850 Da, just over half-way between the monomer and dimer molecular weights. Higher and lower starting concentrations yielded higher and lower average molecular weights, respectively. When the system was modeled as a monomer–dimer equilibrium, a dissociation constant of 40–80 μM was obtained using the known monomeric mass.

Crystal Structure Solution. The b_{62-122} protein crystallized in space group $P2_12_12$ with unit cell dimensions of $a = 35.5$ Å, $b = 41.0$ Å, and $c = 42.3$ Å. The crystals had a rodlike morphology, and the two shortest dimensions (parallel to the *a* and *b* cell axes) rarely exceeded 0.08 mm; nevertheless, they diffracted to 2.2–2.5 Å using a rotating anode source and better than 1.6 Å resolution using a synchrotron source (Tables 1 and 2). The "wild-type" b_{62-122} construct is devoid of both methionine and cysteine. To obtain heavy-atom derivatives, we took advantage of three single cysteine mutants that had been previously characterized (*9*–*11*): b_{62-122}A68C, b_{62-122}A92C, and b_{62-122}A103C. All three constructs crystallized isomorphously with wild-type b_{62-122}, and all three crystals reacted with ethylmercury phosphate (EMP) to provide useful heavy-atom derivatives (Table 2). Isomorphous and/or anomalous difference Patterson maps were resolved in each case, and the derivatives were placed on a common origin. Phase combination using the three derivatives resulted in an overall figure of merit of 0.76 to 2.3 Å resolution (Table 2). The initial experimental electron-

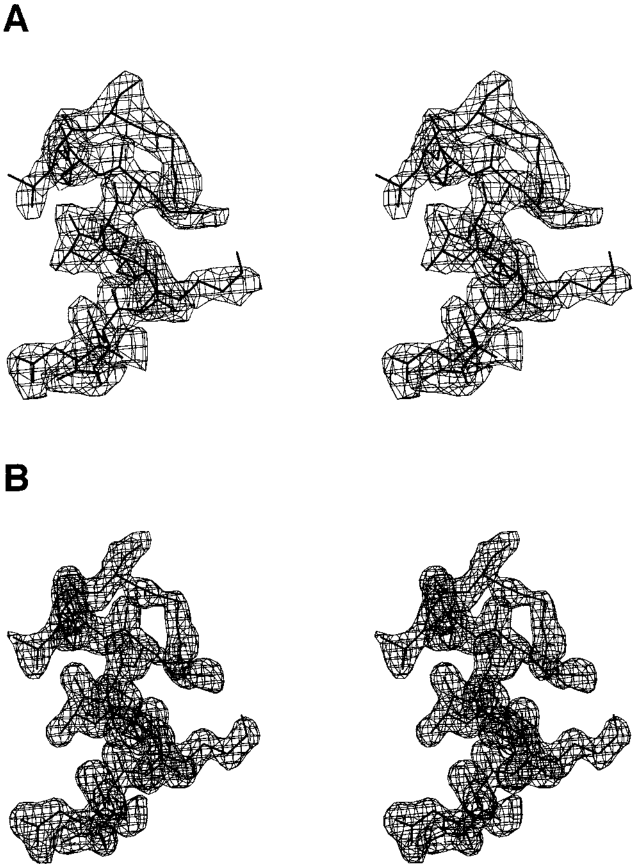

FIGURE 2: Electron density for the b_{62-122} structure. (A) Residues 112–122 (sequence ERKRAREELR) of the final refined b_{62-122} model are illustrated with the initial MIR electron density map, calculated with phases to 2.3 Å and contoured at 1σ. (B) The same residues are shown with a σ_A-weighted (*27*) $2F_{obs} - F_{calc}$ electron density map contoured at 1.2σ using data to 1.55 Å.

Table 3: Refinement Statistics

resolution (Å)	29.4−1.55
reflections ($F \geq 0$)	9325
atoms modeled (protein/water)	494/54
R/R_{free}	0.282/0.313
rms deviations from ideal values	
bond lengths (Å)	0.005
bond angles (deg)	0.7
dihedral angles (deg)	13.1
improper angles (deg)	0.63
mean B values	
overall (Å^2)	29.0
protein main-chain atoms (Å^2)	23.5
protein side chain atoms (Å^2)	30.3
solvent (Å^2)	39.1

thermal factor restraints	rms	target
main-chain bond (Å^2)	1.36	1.50
main-chain angle (Å^2)	1.90	2.00
side-chain bond (Å^2)	3.36	2.00
side-chain angle (Å^2)	5.50	2.50

density map was unambiguous and showed clearly an extended helix comprising residues 68−122. The density of several well-defined side chains, for example, R113, R117, and R121 (Figure 2A), was used to place the sequence in register, and a complete model was built and refined against the 1.55 Å native data set (Figure 2B and Table 3). It is a simple structure consisting of a single, unbroken and almost straight α helix.

We were unable to refine the structure beyond an R_{free} of 0.31. To ensure that b_{62-122} was correctly positioned in the unit cell, we carried out difference Fourier analyses using diffraction data from the cysteine mutants (Table 4). The final refined structure, without crystallographic waters, was subjected to rigid body refinement against data from each of the cysteine-containing b_{62-122} constructs, and then σ_A-weighted (*27*) $F_{\text{obs}} - F_{\text{calc}}$ maps were calculated. The largest difference Fourier peaks occur at positions one would expect for the sulfur and/or mercury atoms. The failure of the b_{62-122} refinement to converge below an R_{free} of 0.31 is likely due to static disorder within the crystals. The b_{62-122} helices are arranged in the crystal such that the C terminus of one polypeptide is approximately one helical turn from the N terminus of the next polypeptide; that is, the individual helices arrange themselves in tandem to form a "pseudo-continuous" helix. The crystal is formed with layers of these helices, which stack in the direction of the crystallographic *b* axis (Figure 3). The helices in each layer are parallel to one another, and they make contact and cross those of the next layer at an angle of approximately 45°. We believe that the disorder within the crystals is due to some minor proportion of the helices packing such that they are "out of phase" with others in the crystal; that is, the sequence is shifted along the helical axis. This would have little effect on the backbone of the structure but would place side chains of the shifted helices in the wrong position. In support of

Table 4: Difference Fourier Analysis of b_{62-122} Cysteine Mutants

data set	R/R_{free}	coordinates of Ala CB[a]	coordinates of peak	peak height[b]
A68C	32.8/32.7	(−14.0, 0.7, −26.6)	(−13.5, −0.4, −23.4)	12.3 (5.1)
A68C-EMP	37.8/37.9	(−13.9, 0.7, −26.6)	(−13.4, −0.5, −23.5)	19.5 (4.3)
A92C	34.5/34.6	(2.7, 9.2, 4.9)	(3.2, 9.7, 3.5)	6.1 (4.5)
A92C-EMP	37.9/38.1	(2.6, 9.2, 4.9)	(4.4, 10.7, 7.2)	18.4 (7.0)
A103C	34.9/36.7	(8.3, 8.8, 20.9)	(9.0, 9.6, 19.9)	4.4 (4.3)
A103C-EMP	37.8/38.6	(8.1, 8.7, 21.0)	(9.5, 10.4, 23.8)	8.3 (5.0)
native 2	31.1/32.7	(−13.9, 0.7, −26.6) (2.4, 9.2, 4.9) (8.1, 8.8, 20.9)	(3.2, 9.7, 3.5)	4.7 (4.7)

[a] These are the coordinates for the β carbon of Ala68, Ala92, or Ala103 of our final refined structure after rigid body refinement against the given data set. [b] Numbers in parentheses indicate height of second highest peak.

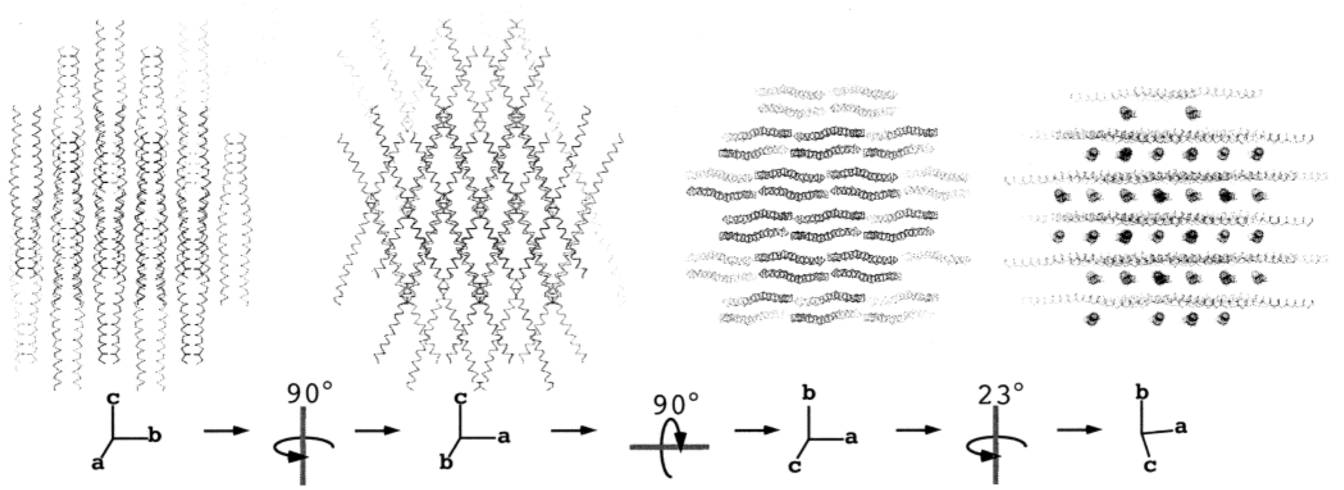

FIGURE 3: Crystal packing of b_{62-122}. The crystal packing of b_{62-122} is illustrated, beginning at the left, with the *a* axis perpendicular to the plane of the paper. Moving to the right, consecutive 90° rotations illustrate the crystal packing with the *b* and *c* axes perpendicular to the plane of the paper. In the far right, the figure has been rotated 23° around the *b* axis to illustrate how the helices in each layer are arranged parallel to one another. Note that crystal growth was highly asymmetric; the crystals were long rods in the direction of rapid crystal growth parallel to the *c* axis.

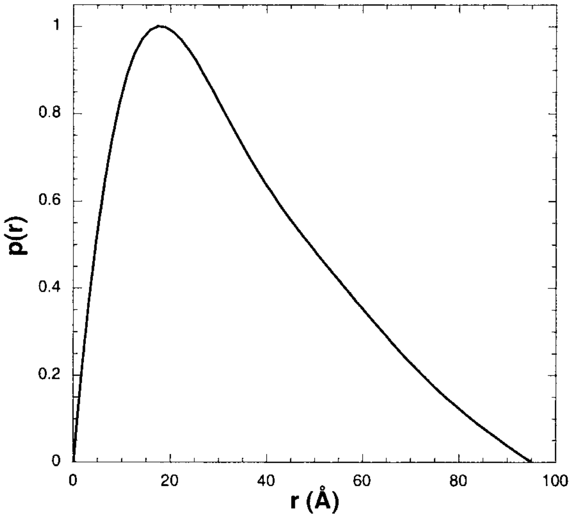

FIGURE 4: Distance distribution function of b_{62-122}. SAXS data from b_{62-122} at 12 mg mL^{-1} were collected in the momentum transfer range 0.003 Å^{-1} < S < 0.035 Å^{-1}. The distance distribution function was calculated from these data using the indirect transform method implemented in the program GNOM (*32*).

this idea, we note that side chain *b* factors yield through-bond and through-angle rms values much greater than typical target values, whereas the main-chain *b* factors refine to rms values below the target (Table 3).

The b_{62-122} protein did not crystallize as a dimer, which is likely because of the high concentrations of 2-propanol (45%) and MPD (30%) in the mother liquor. Long, isolated α helices are not commonly found in crystal structures, and it seems rather remarkable that the b_{62-122} polypeptide crystallized in this fashion; however, there is nothing unusual about the properties of the b_{62-122} helix. For example, Blundell et al. (*28*) showed that an α helix in a hydrophobic environment adopts average φ and ψ values of −59° and −44°, whereas in a solvent-exposed hydrophilic environment, the φ and ψ values are −66° and −41°. Consistent with its high degree of solvent exposure, the isolated b_{62-122} helix has average φ and ψ values of −64° and −41°, respectively. Twenty of the crystallographic water molecules are hydrogen-bonded to backbone carbonyl groups. This type of interaction has been shown to cause the carbonyl group to tilt outward from the helix axis, increasing the average O_i to N_{i+4} distance from 2.91 to 3.09 Å and decreasing the average $C_I-O_i-N_{i+4}$ angle from 157° to 148° (*28, 29*). For b_{62-122}, the average O_i-N_{i+4} distance is 3.0 Å while the average $C_i-O_i-N_{i+4}$ angle is 153°, and the carbonyl groups for which a crystallographic water molecule is present are not significantly different from those with no crystallographic water. It may be that the relatively low polarity of the solvent coupled with the high degree of solvent exposure causes the backbone carbonyl groups to assume intermediate values.

Solution Structure of b_{62-122}. Small-angle X-ray scattering (SAXS) was used to investigate the solution structure of b_{62-122} in aqueous buffer comprising 20 mM sodium acetate and 20 mM NaCl, pH 5.0. We measured SAXS in the momentum transfer range 0.003 Å^{-1} < S < 0.035 Å^{-1} from b_{62-122} at a concentration of 12 mg mL^{-1}. This protein concentration was designed to maximize the amount of dimer in solution (approximately 85−90%) and yet avoid inter-

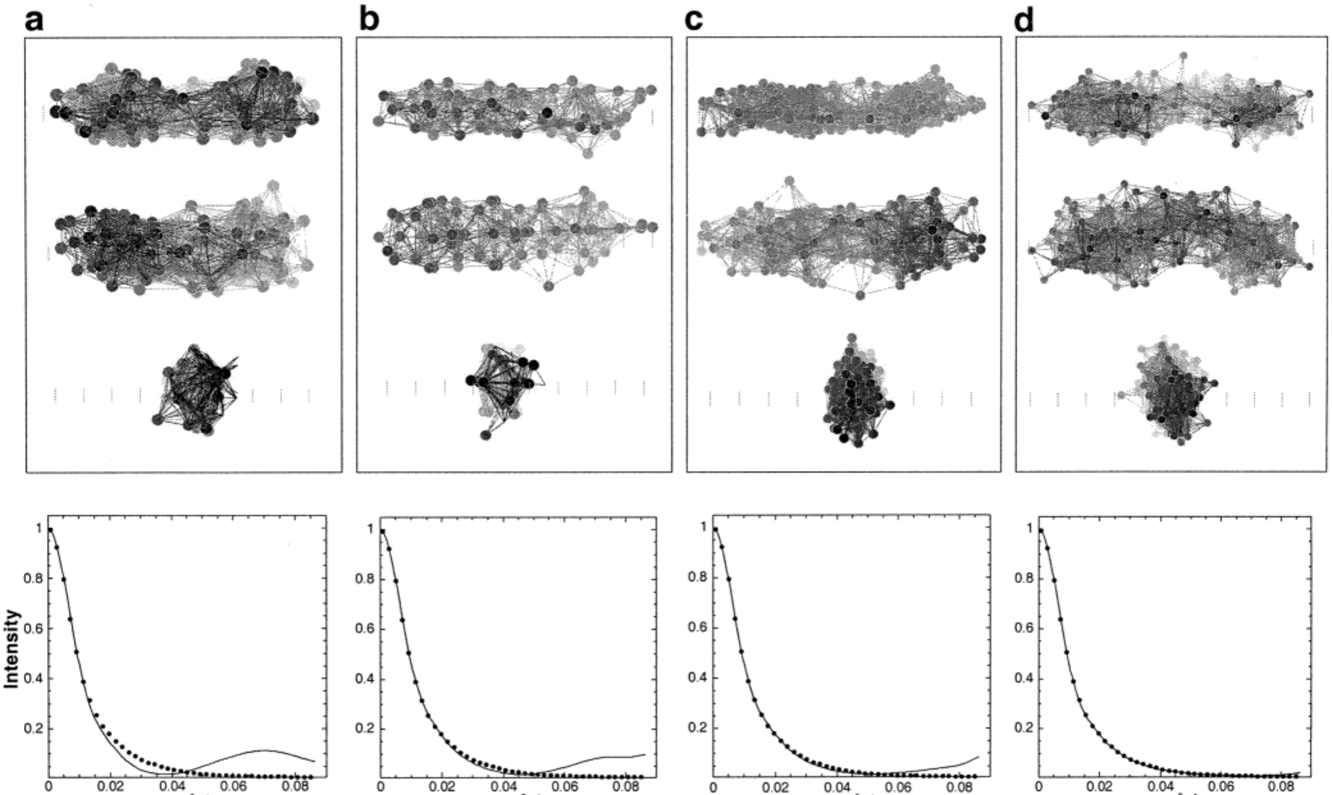

FIGURE 5: Shape of b_{62-122} in solution. The programs Saxs3D and xlattice (*30*) were used to calculate shapes from regular SAXS data (0 Å^{-1} < S < 0.08 Å^{-1}) using lattice spacings of (a) 1.8 Å, (b) 1.6 Å, (c) 1.4 Å, or (d) 1.2 Å. In each case, 10 structures were calculated by successive runs of Saxs3D and then superimposed using xlattice. The graphs at the bottom of each panel show the experimental data (dotted curve) with a curve (solid) that represents the average calculated scattering from each set of 10 superimposed structures.

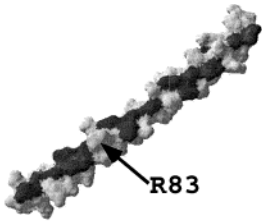

FIGURE 6: Hydrophobic strip of b_{62-122}. The molecular surface of the b_{62-122} monomer is black for hydrophobic residues and gray for all others. The position of the R83 side chain is indicated by an arrow. The hydrophobic strip was used as the dimer interface to orient two b_{62-122} monomers to yield a dimer with a right-handed superhelical twist.

particle interference, which affects the very low-angle region. Under these conditions, the molecule has a maximal dimension of 95 Å and a radius of gyration of 27 Å. For comparison, a globular protein such as lysozyme, with a molecular weight similar to that of the b_{62-122} dimer, has a maximal dimension of 45 Å and a radius of gyration of 15 Å. The extended nature of the b_{62-122} protein in solution is also evident from the distance distribution function (Figure 4), which can be viewed as a histogram of interatomic distances within the molecule. For a globular protein, the distribution is expected to be roughly Guassian; for more extended, rodlike molecules, the distribution becomes skewed toward smaller interatomic distances. The highly skewed distance distribution function of the b_{62-122} dimer represents an extreme case.

We used our SAXS data and the program Saxs3D (*30*) to determine, ab initio, a shape for the b_{62-122} molecule in solution. This process (used for a completely different protein) is described in greater detail in a previous manuscript (*31*). Briefly, Saxs3D is used to construct low-resolution "bead models" for the protein based on SAXS data. The models obtained are not absolutely unique, and therefore, to extract the "essential" or "common" shape information encoded in the scattering curve, individual models are superimposed and contrast-filtered using the program xlattice (*30*). The bead size influences the outcome; larger beads correspond to fewer parameters, and therefore, the fit to the experimental data is generally not as good as for a smaller bead size. On the other hand, if the bead size is too small, there will be too many parameters and the algorithm fails to converge. It is important to note that the shape simply distinguishes the protein, a region of relatively high electron density, from the solvent but does not provide any information on the finer structural features of the protein.

The Saxs3D algorithm requires data from $S = 0.0$ Å^{-1} to the highest angle measured, preferably at $S = 0.06$ Å^{-1} or greater. We merged two data sets to cover the large momentum transfer range required. The first data set (0.02 Å^{-1} $< S <$ 0.03 Å^{-1}) was recorded from a 12 mg mL^{-1} solution of b_{62-122}, using a 3 m sample-to-detector distance (as described), and the second data set, 0.015 Å^{-1} $< S <$ 0.085 Å^{-1}, was recorded from a 25 mg mL^{-1} solution of b_{62-122} using a 1.2 m camera. The two data sets were scaled and merged using the program GNOM (*32*); after scaling and merging, a regularized scattering curve (0.0 Å^{-1} $< S <$ 0.085 Å^{-1}) was calculated and these data were used for shape determination by Saxs3D. Ten independent models were calculated for each of four lattice spacings (bead diameters): 18, 16, 14, and 12 Å. Each set of 10 models was superimposed using the program xlattice (*30*). In this way, "average" structures were obtained that illustrate the conserved low-resolution structure of the b_{62-122} dimer (Figure 5). The essential shape (which is rodlike with dimensions 20 Å × 30 Å × 95 Å) is encoded in the lower angle region of the scattering curve, a region for which the 16 Å lattice spacing was sufficient to match the scattering data.

Right-Handed Coiled-Coil Model for the b_{62-122} Dimer. The shape of the b_{62-122} dimer obtained from SAXS suggested that the crystal structure of the b_{62-122} monomer could be used directly to construct a model for the homodimer. Most of the hydrophobic residues in the b_{62-122} monomer are arranged in a strip along the surface of the α helix (Figure 6). In constructing a model for the b_{62-122} dimer, we assumed that this strip of hydrophobic residues constitutes the dimer interface, and we visually aligned these strips, adjusting the relative orientation of the protomers to maximize intermolecular contacts. Some side chain conformations were adjusted to remove severe steric clashes, but the overall backbone conformation was not altered. Because the strip moves around the helix in a right-handed sense, our model for the b_{62-122} dimer has a right-handed superhelical twist.

A parallel, two-stranded, right-handed coiled-coil structure has never been observed. However, the prediction of right-handed coiled-coil structures (*33, 34*) has been confirmed by the characterization of both natural (*35*) and designed (*36*) four-stranded right-handed helical bundles. To form a right-handed coiled coil, a polypeptide is expected to contain an 11-residue repeating motif that is characterized by hydrophobic residues at the *a* and *h* positions (Figure 7). This type of motif is termed an undecad repeat and is distinguished from the heptad repeat associated with typical left-handed coiled coils (*34*). As can be seen in Figure 7, the undecad repeat in the dimerization domain of *b* subunit sequences is

```
Heptad repeat        cdefgabcdefgabcdefgabcdefgabcdefgabcd                abcdefgabcdefgabcd
Undecad repeat       defghijkabcdefghijkabcdefghijkabcdefghijkabcdefghijkabcdefghijkabcdefghijkabc
E. coli           53 DLDLAKASATDQLKKAKAEAQVIIEQANKRRSQILDEAKAEAEQERTKIVAQAQAEIEAERKRAREELRKQVAILAV 129
T. maritima       55 EAEKMRSEAERFLSEARQRADEIVESARKEAEAIVEEAREKAKKEAQNIVESAKTQIEVEYKKALEQVQERAAELSV 131
P. modestum       61 MAAKANGEAQGIVKSAKTEANEMLLRAEKKADERKETILKEANTQREKMLKSAEVEIEKMKEQARKELQLEVTDLAV 137
T. ferrooxidans   56 EMALAQKRATELVREAKDKAAEIIANAERRGVELREEAQGKAREEADRIIASARAEIDVETNRAREVLRGQVVELVV 132
B. caldotenax     68 EAEKLLEEQRELMKQSRQDDEALIENARKLAQEQKEQIVASARGQAERVKEAAKKEIEREKEQAMAALREQVASLSV 144
B. subtilis       63 EAQQLIEEQRVLLKEARQESQTLIENAKKLGEKQKEEIIQAARAESERLKEAARTEIVKEKEQAVSALREQVASLSV 139
E. faecalis       64 NSAKMEQEREQQLLASRSDAADIIKNAKESGELSRQNILKETQEEVARLKSKAQTDIMLERDTALNSVKDDADLSLQ 140
Synechocystis b   73 KSAQILAEEEKKLAQAKAEAARIVQEAGQRAEVAKQEIATQTEADLRRMQEAAAQDLGAEQERVIAELKRRIAEQAV 149
Synechocystis b'  54 KAKAITQEYEQQITDARRQSQAVIADAQAEARRLAAEKIAEAQRESQRQKETAAQEIEAQRQSALSSLEQEVAALSN 130
```

FIGURE 7: Sequence alignment of *b* subunit dimerization domains. The *b* sequences aligned above are compared to the heptad and undecad positions of a theoretical coiled coil. The *a* and *d* positions of the heptad repeat, which are typically hydrophobic residues in a left-handed coiled-coil motif, are underlined. Hydrophobic residues in *a* and *h* positions of the right-handed coiled-coil undecad repeat (shaded gray) show substantial conservation across species. In the *E. coli* sequence, the R83 residue (shaded black) disrupts the pattern.

better maintained than the heptad repeat, which is largely absent from the middle portions of the sequences. Thus, our model for the b_{62-122} dimer is consistent with *b* subunit sequences from *E. coli* and related organisms.

Mutational Evidence for the b_{62-122} Dimer Model. From both the structure of b_{62-122} (Figure 6) and the sequence alignment of ATP synthase *b* subunits (Figure 7), it is clear that the hydrophobic strip, represented by the undecad repeat in the primary sequence, is interrupted at several positions. In particular, R83 occupies the "*a*" position of the undecad repeat and clearly disrupts the hydrophobic strip (Figure 6); in fact, this residue is present as alanine in a number of the *b* sequences (Figure 7). Given our proposed right-handed coiled-coil model, we hypothesized that mutation of R83 to alanine should increase the stability of the b_{62-122} dimer.

As the first test of this idea, an R83A mutation was inserted into the b_{53-122} construct that has been extensively studied through both analytical ultracentrifugation and circular dichroism spectroscopy (*9, 26*). The CD spectrum of this protein at low temperatures shows strong, nearly equal minima at 222 and 208 nm, characteristic of an α-helical coiled coil. At higher temperatures or low protein concentrations, the ellipticity declines in a manner indicative of an equilibrium between a folded, helical dimer and an unfolded monomer (*26*). As can be seen in Figure 8A, the melting curve monitored by CD as a function of temperature was shifted to higher temperature by the R83A mutation, with the midpoint increasing by about 7 °C. Sedimentation equilibrium analysis was carried out to ensure that this change reflected the higher stability of the dimer. In Figure 8B, analysis of the effect of temperature on the average molecular weight confirmed that the R83A mutation made dimerization more thermostable, supporting the interpretation of the CD melting curve as characteristic of a transition between dimeric and monomeric species. Sample data collected at 35 °C (Figure 8C) illustrate the notably steeper concentration gradients formed by the R83A mutant at temperatures where partial melting had occurred.

A similarly dramatic stabilizing effect of the R83A mutation on dimerization in the 62−122 construct was seen in plots of sedimentation coefficient versus protein concentration (Figure 1) and melting curves in the CD (Figure 9). The sedimentation coefficient of 1.24−1.25 for this construct implies a frictional ratio of 1.6. As controls for the possibility that the greater stability of b_{62-122}R83A might simply reflect the general tendency of alanine residues to stabilize helices rather than being specific to the 83 position, arginine residues at positions 82 and 98 were also changed to alanine. Arg-82 is of particular interest because it occupies the "*d*" position of the heptad repeat (Figure 7) and would be present in the dimer interface of a left-handed coiled coil. Rather than having any stabilizing effect, however, each of these mutations weakened the structure and lowered the melting point. These results support the right-handed model with preference for alanine residues in the *a* and *h* positions of the undecad and argue against a left-handed coiled coil. It should be noted in this regard that Sorgen and co-workers (*37*) found that mutation of Ala-79, which occupies an *h* position in the undecad, to leucine destabilized dimerization. This observation highlights the fact that positions *a* and *h* in the undecad are often occupied by alanine residues and not simply by hydrophobic residues. The reason alanine residues are preferred at these positions is not clear at the present time. Our results with the R82A and R98A mutations further

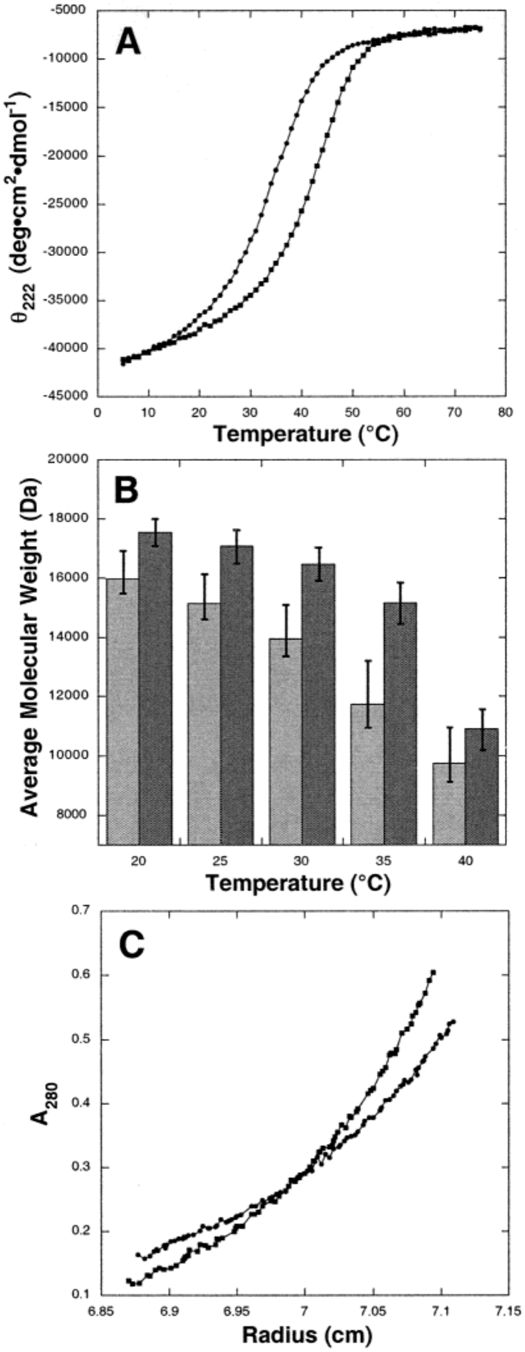

FIGURE 8: Effect of the R83A mutation on stability of b_{53-122}. Analyses were carried out by circular dichroism or sedimentation equilibrium ultracentrifugation in a buffer containing 25 mM sodium phosphate, pH 7.0, and 50 mM NaCl. (A) Thermal denaturation was monitored by circular dichroism at 222 nm as a function of temperature. Polypeptide concentrations were 0.89 mg of b_{53-122} per milliliter (circles) or 0.82 mg of b_{53-122}R83A per milliliter (squares). (B) Average molecular weights for wild-type b_{53-122} and b_{53-122}R83A were determined by sedimentation equilibrium analysis at temperatures from 20 to 40 °C. Initial protein concentrations were 0.3 mg/mL for either b_{53-122} or b_{53-122}R83A, and the rotor speed was 25 000 rpm. Cells were scanned at 280 nm after equilibrium was reached at each temperature. Triplicate data sets were analyzed for the best fit to a single species to obtain average molecular weights. The error bars show the 95% confidence interval. (C) Sample sedimentation equilibrium data sets collected after equilibration at 35 °C, illustrating the steeper gradient formed by b_{53-122}R83A (squares) compared to wild-type b_{53-122} (circles).

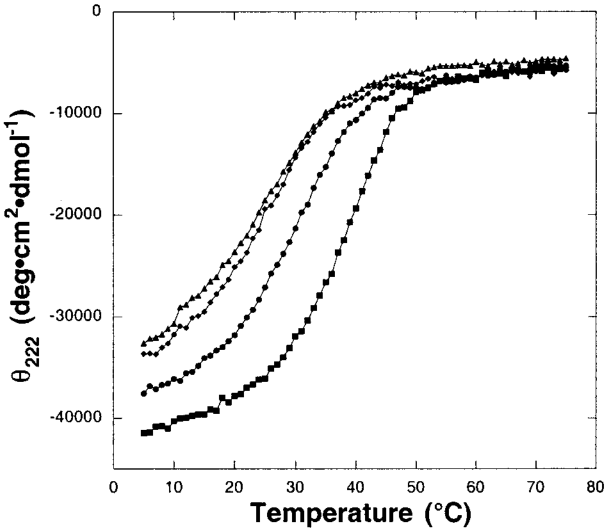

FIGURE 9: Effect of arginine-to-alanine mutations on thermal stability of b_{62-122}. Thermal denaturation profiles of wild-type or mutant b_{62-122} were obtained by circular dichroism at 222 nm as a function of temperature, using methods described under Experimental Procedures. Each polypeptide was present at a concentration of 1.4 mg/mL in 25 mM sodium phosphate buffer, pH 7.0: wild-type b_{62-122}, circles; b_{62-122}R82A, triangles; b_{62-122}R83A, squares; b_{62-122}R98A, diamonds.

suggest that charged residues, such as arginine, at other positions may be involved in electrostatic interactions critical to the stability of the structure.

SAXS from R83A: Evaluation of the b_{62-122} Dimer Model in Solution. We collected SAXS data from b_{62-122}R83A to ensure that the mutation did not drastically alter the structure but simply increased the stability of the b_{62-122} "wild-type" structure. In addition, SAXS measurements from b_{62-122}R83A have the advantage that this protein is close to 100% dimer at the concentrations used for SAXS experiments. These data were collected at BioCAT beamline 18ID of the Advanced Photon Source, and the intensity of the X-ray beam, combined with the sensitivity of the detector, allowed us to collect strong scattering data to very high values of momentum transfer. As can be seen in Figure 10A, the scattering from the R83A mutant was essentially identical to that of wild-type b_{62-122}.

We used data from b_{62-122}R83A to refine our model for the b_{62-122} dimer. Minor adjustments in the relative positions of the helices, combined with changes in side chain rotomers, improved the fit of the model to the SAXS data ($\chi^2 = 5.3$; Figure 10B). This model for the dimer (Figure 10C) makes sense chemically; the hydrophobic strips of each protomer are in close contact and are sequestered from solvent, and there are neither bad contacts nor unreasonable side chain conformations. We also wanted to evaluate how a left-handed helix would fit the b_{62-122}R83A data. To produce a left-handed model, the b_{62-122} sequence was threaded onto a left-handed coiled-coil structure (*38*). Unfortunately, this model yielded only a slightly worse fit to the data ($\chi^2 = 6.1$), and we are therefore unable to rule out a typical left-handed coiled-coil structure on the basis of the SAXS data alone. To summarize, the b_{62-122} dimer, with or without the R83A mutation, is a rodlike structure, and our right-handed coiled-coil model is consistent with the SAXS data. Details concerning backbone conformation, side chain packing in the dimer interface, ionic interactions, and so on will have to await the high-resolution crystal structure determination of a b-subunit dimer.

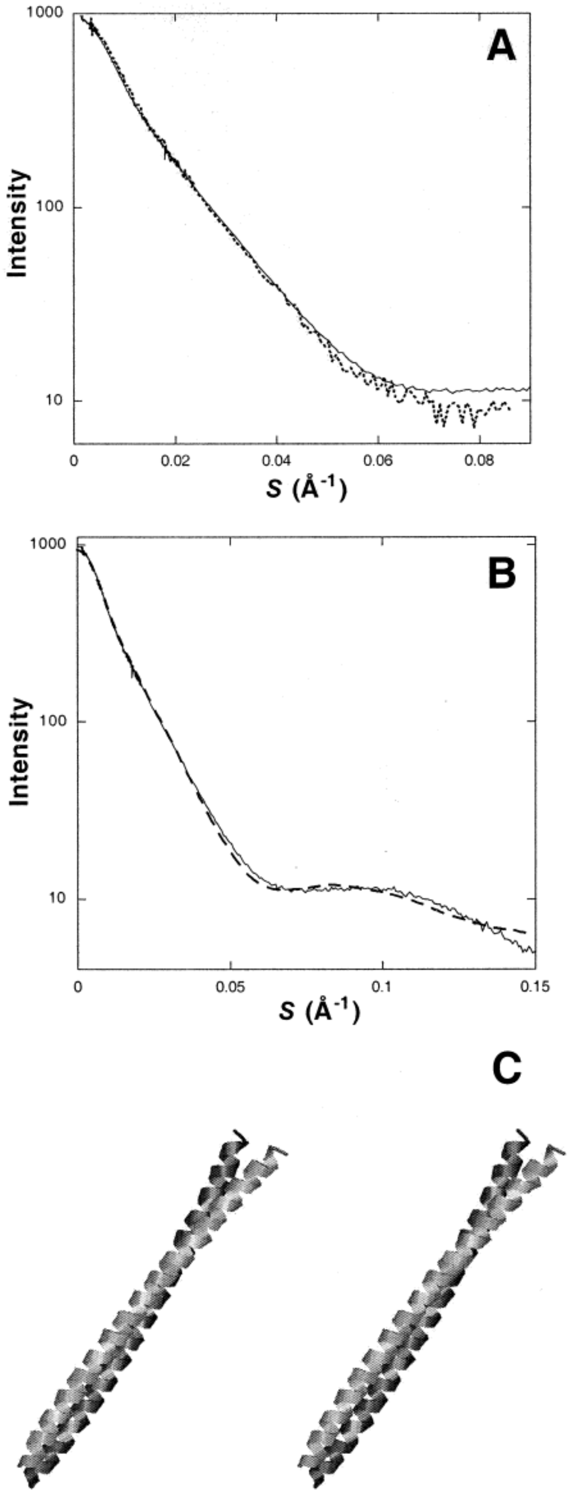

FIGURE 10: SAXS of the R83A mutant. (A) SAXS data collected from wild-type b_{62-122} (dotted curve) are compared to data collected from b_{62-122}R83A, which forms a much tighter dimer (solid curve). (B) Theoretical X-ray scattering from the right-handed coiled-coil model (with an R83A mutation; dashed curve) was calculated using the program CRYSOL (*25*) and fit to data collected from b_{62-122}R83A (solid curve) to very high values of momentum transfer ($S = 0.15$ Å^{-1}). (C) Structure of the final b_{62-122} dimer model.

CONCLUSION

The ab initio determination of a low-resolution structure for the b_{62-122} dimer yielded a rodlike particle approximately

95 Å in length, which is consistent with a fully extended coiled coil. We resolved the crystal structure of the isolated b_{62-122} monomer, and using a simple assumption that the dimer interface will be formed from the strip of hydrophobic residues in this structure, we have constructed a model for the b_{62-122} dimer that provides a good fit to solution scattering data. On the basis of the model structure, we predicted that arginine 83 would be present in the dimer interface, and its conversion to alanine would therefore result in an increase in stability of the dimer. This prediction was correct; the mutation produced a dramatic increase in the stability of two dimerization domain constructs, b_{53-122} and b_{62-122}.

Our right-handed coiled-coil structure is also consistent with biophysical data (*26*). In particular, *b* subunit dimerization domain constructs, when compared with other coiled coils, are relatively unstable with a low heat capacity difference between the folded and unfolded forms (ΔC_p). ΔC_p should be roughly proportional to the amount of hydrophobic surface exposed on unfolding. In our dimer model, the amount of buried surface is less than 12 Å^2/residue on average, compared to over 18 Å^2/residue for the rod domain of cortexillin, an example of a left-handed coiled-coil structure (*38*).

Our model for the b_{62-122} dimer structure satisfies most of the available experimental evidence, and we can see no reasonable alternative. The reason for such an uncommon structure is not obvious at the present time. However, it has been proposed that elastic energy is able to accumulate in ATP synthase (*39*), and this unusual structure may provide a mechanism for energy storage during coupled rotation.

ACKNOWLEDGMENT

We thank Marie Fraser for useful discussions and David Cadotte for technical assistance in the purification of b_{62-122}.

REFERENCES

1. Walker, J. E., Ed. (2000) *Special Issue: The Mechanisms of F_1F_0-ATPase, Biochim Biophys Acta 1458*, Elsevier Science B.V., Amsterdam.
2. Nakamoto, R. K., Ketchum, C. J., and al-Shawi, M. K. (1999) *Annu. Rev. Biophys. Biomol. Struct. 28*, 205−234.
3. Weber, J., and Senior, A. E. (1997) *Biochim. Biophys. Acta 1319*, 19−58.
4. Junge, W., Lill, H., and Engelbrecht, S. (1997) *Trends Biochem. Sci. 22*, 420−423.
5. Jiang, W., Hermolin, J., and Fillingame, R. H. (2001) *Proc. Natl. Acad. Sci. U.S.A. 98*, 4966−4971.
6. Kersten, M. V., Dunn, S. D., Wise, J. G., and Vogel, P. D. (2000) *Biochemistry 39*, 3856−3860.
7. Dunn, S. D., Revington, M., Cipriano, D. J., and Shilton, B. H. (2000) *J. Bioenerg. Biomembr. 32*, 347−355.
8. Sambrook, J., Fritsch, E. F., and Maniatis, T. (1989) *Molecular Cloning: A Laboratory Manual* 2nd ed., Cold Spring Harbor Laboratory Press, Cold Spring Harbor, NY.
9. Revington, M., McLachlin, D. T., Shaw, G. S., and Dunn, S. D. (1999) *J. Biol. Chem. 274*, 31094−31101.
10. McLachlin, D. T., and Dunn, S. D. (1997) *J. Biol. Chem. 272*, 21233−21239.
11. McLachlin, D. T., Coveny, A. M., Clark, S. M., and Dunn, S. D. (2000) *J. Biol. Chem. 275*, 17571−17577.
12. Cohn, E. J., and Edsall, J. T. (1943) in *Proteins, Amino Acids, and Peptides*, pp 157−161, Reinhold, NY.
13. Philo, J. S. (1997) *Biophys. J. 72*, 435−444.
14. Otwinowski, Z., and Minor, W. (1997) in *Methods in Enzymology 276* (Carter, C. W. J., and Sweet, R. M., Eds.) pp 307−326, Academic Press, New York.
15. CCP4 (1994) *Acta Crystallogr. D50*, 760−763.
16. Jones, T. A., Bergdoll, M., and Kjeldgaard, M. (1990) in *Crystallographic and Modeling Methods in Molecular Design* (Bugg, C. E., and Ealick, S. E., Eds.) pp 189−195, Springer-Verlag, New York.
17. Brunger, A. T., Adams, P. D., Clore, G. M., DeLano, W. L., Gros, P., Grosse-Kunstleve, R. W., Jiang, J. S., Kuszewski, J., Nilges, M., Pannu, N. S., Read, R. J., Rice, L. M., Simonson, T., and Warren, G. L. (1998) *Acta Crystallogr., Sect. D: Biol. Crystallogr. 54*, 905−921.
18. Guex, N., and Peitsch, M. C. (1997) *Electrophoresis 18*, 2714−2723.
19. Koch, M. H. J., and Bordas, J. (1983) *Nucl. Instrum. Methods 208*, 461−469.
20. Boulin, C. J., Kempf, R., Gabriel, A., and Koch, M. H. J. (1988) *Nucl. Instrum. Methods A269*, 312−320.
21. Boulin, C., Kempf, R., Koch, M. H. J., and McLaughlin, S. (1986) *Nucl. Instrum. Methods A249*, 399−407.
22. Hammersley, A. P., Svensson, S. O., Hanfland, M., Fitch, A. N., and Häusermann, D. (1996) *High-Pressure Res. 14*, 235−248.
23. Hammersley, A. P. (1997) FIT2D: An Introduction and Overview, ESRF Internal Report ESRF97HA02T ESRF, Grenoble, France.
24. Hammersley, A. P. (1998) FIT2D V9.129 Reference Manual V3.1, ESRF Internal Report ESRF98HA01T ESRF, Grenoble, France.
25. Svergun, D. I., Barberato, C., and Koch, M. H. J. (1995) *J. Appl. Crystallogr. 28*, 768−773.
26. Revington, M., Dunn, S. D., and Shaw, G. S. (2002) *Protein Sci., 11*, 1227−1238.
27. Read, R. J. (1986) *Acta Crystallogr. A42*, 140−149.
28. Blundell, T., Barlow, D., Borkakoti, N., and Thornton, J. (1983) *Nature 306*, 281−283.
29. Barlow, D. J., and Thornton, J. M. (1988) *J. Mol. Biol. 201*, 601−619.
30. Walther, D., Cohen, F. E., and Doniach, S. (2000) *J. Appl. Crystallogr. 33*, 350−363.
31. Dempsey, B. R., Economou, A., Dunn, S. D., and Shilton, B. H. (2002) *J. Mol. Biol. 315*, 831−843.
32. Semenyuk, A. V., and Svergun, D. I. (1991) *J. Appl. Crystallogr. 24*, 537−540.
33. Peters, J., Baumeister, W., and Lupas, A. (1996) *J. Mol. Biol. 257*, 1031−1041.
34. Lupas, A. (1996) *Trends Biochem. Sci. 21*, 375−382.
35. Stetefeld, J., Jenny, M., Schulthess, T., Landwehr, R., Engel, J., and Kammerer, R. A. (2000) *Nat. Struct. Biol. 7*, 772−776.
36. Harbury, P. B., Plecs, J. J., Tidor, B., Alber, T., and Kim, P. S. (1998) *Science 282*, 1462−1467.
37. Sorgen, P. L., Bubb, M. R., McCormick, K. A., Edison, A. S., and Cain, B. D. (1998) *Biochemistry 37*, 923−932.
38. Burkhard, P., Kammerer, R. A., Steinmetz, M. O., Bourenkov, G. P., and Aebi, U. (2000) *Struct. Fold. Des. 8*, 223−230.
39. Cherepanov, D. A., Mulkidjanian, A. Y., and Junge, W. (1999) *FEBS Lett. 449*, 1−6.

BI025736I